

Supporting Information

Contents

- S1. TGA and DTG of oil palm leaves.
- S2. SEM images and EDX elemental mapping of oil palm leaves.
- S3. EDX elemental mapping of the as-prepared porous carbons.
- S4. X-ray diffraction (XRD) of the Cabokarn.
- S5. CV curves of the as-prepared porous carbons in 1m LiTFSI electrolytes.
- S6. CV curves of the as-prepared materials and the specific capacitance in 1 m LiTFSI electrolyte.
- S7. Nyquist and Bode plots of the as-prepared carbon materials
- S8. CV curves of the as-prepared porous carbons in 20m LiTFSI electrolytes.
- S9. CV curves of the as-prepared materials and the specific capacitance in 20 m LiTFSI electrolyte.
- S10. CV curves of the as-prepared porous carbons in 1 m and 20m LiCl and LiTFSI electrolytes.
- S11. Cycling properties of OPL_KOH12 in 1 m and 20m LiCl and LiTFSI electrolytes
- S12. The calculated specific capacitance versus cycle number in different electrolytes
- S13. Dependence of stored charge versus scan rate in LiCl and LiTFSI electrolytes.
- S14 Cyclic stability of the symmetric coin cells fabricated from the OPL_KOH12 electrode in 20 m LiCl and LiTFSI electrolytes
- S15 The XPS spectra of OPL_KOH samples

Table S1 XPS analysis data of the OPL_KOH materials

Table S2 The values from the fitting equivalent circuits (OPL_KOH12 in LiCl and LiTFSI electrolytes)

Supporting equations

Eq S1 real parts of the complex capacitance calculation.

Eq S2 imaginary parts of the complex capacitance calculation.

Eq S3 capacitance calculation from EIS data.

Figure S1. TGA and DTG of oil palm leaves.

The thermal stability and the decomposition temperatures of oil palm leaves (OPL) were investigated using TGA/DTG as illustrated in Figure S1. In the first stage of OPL decomposition (from room temperature up to 160 °C), a mass loss is due to the evaporation of adsorbed water. The second stage, with a temperature ranging from 230 to 300 °C, corresponds to the decomposition of cellulose and hemicellulose¹. In the third stage, the carbonaceous material that is slowly decomposing (320 and 400 °C).²

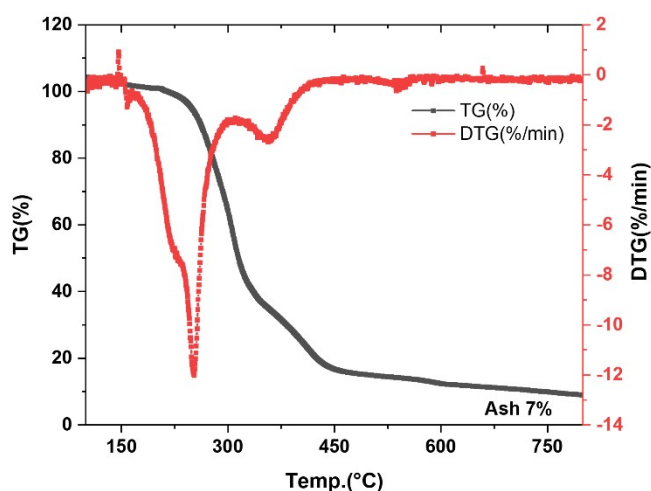
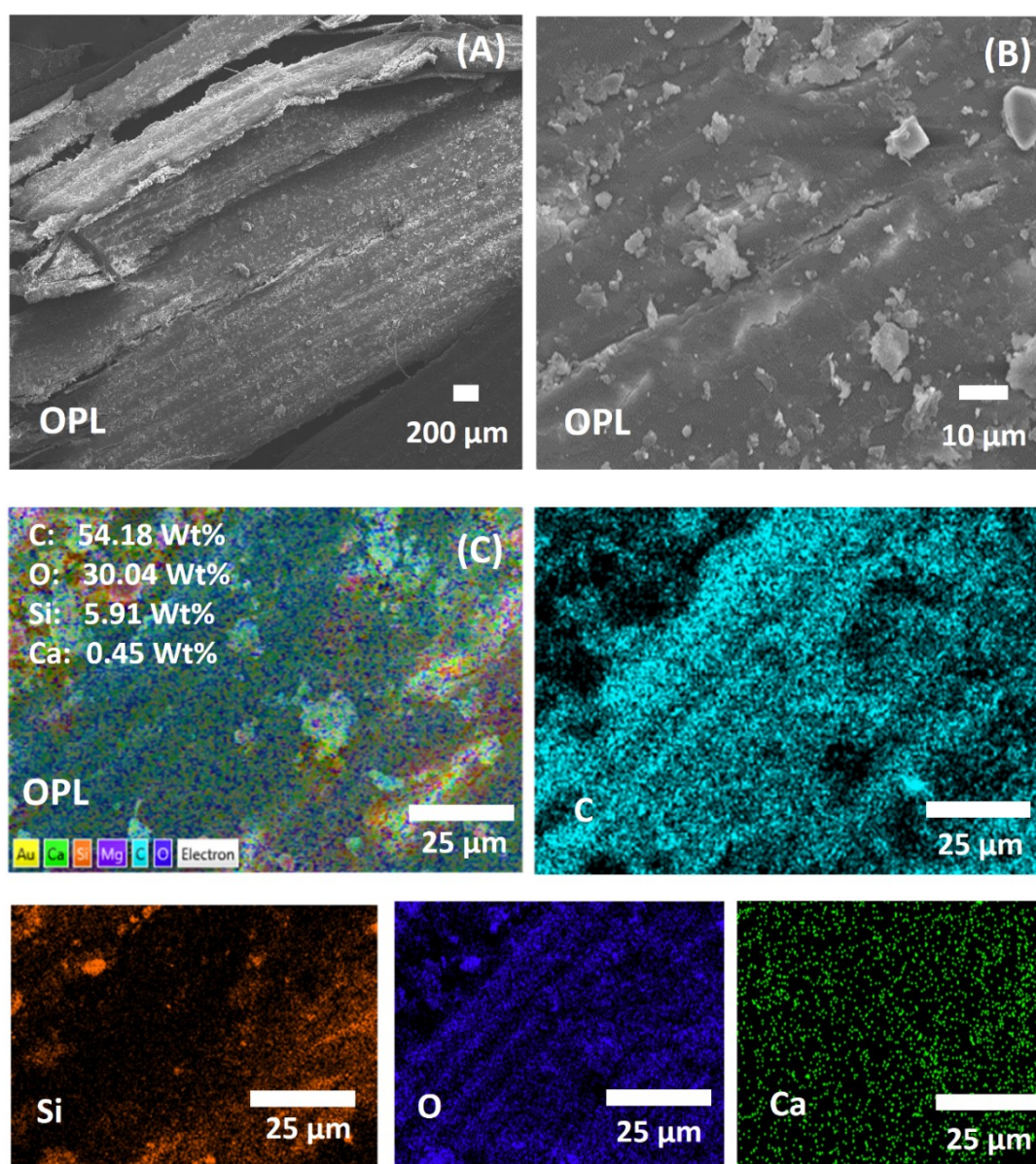


Figure S1. TGA and DTG of OPL.

Figure S2. SEM images and EDX elemental mapping of oil palm leaves.

The SEM images show a smooth surface of oil palm leaves (Figure S2A-B). The EDX elemental mapping confirms that OPL consists of carbon which represents cellulose and minerals (including Si 5.91%, Ca 0.45%, and Mg 0.36%) in the oil palm leaves, in agreement with the previous TGA result.



Figure

re S2. (A-B) SEM images of OPL. (C) EDX mapping of OPL.

Figure S3. EDX elemental mapping of the as-prepared porous carbons.

The elemental compositions of as-prepared carbon are shown in Figure S3. The as-prepared carbon materials contain a high amount of carbon, oxygen and silicon. After the KOH activation, the percentage of carbon increases while other elements are moderately eliminated.

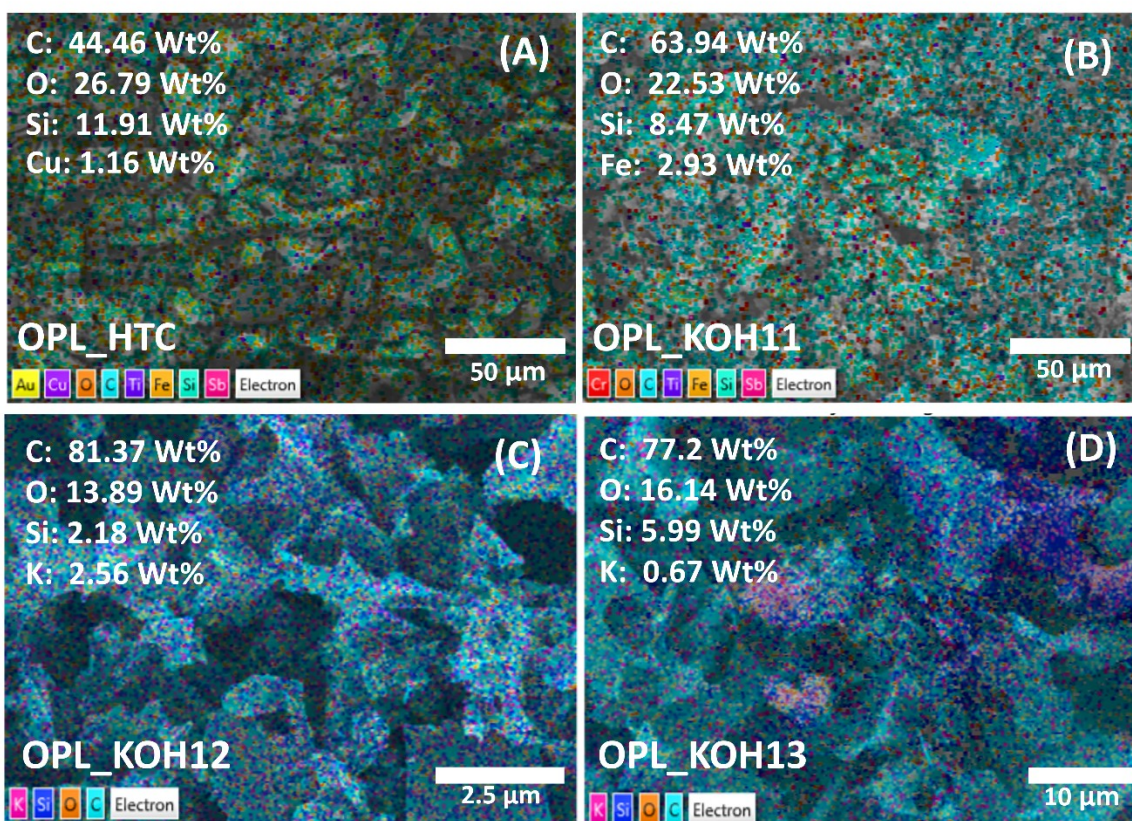
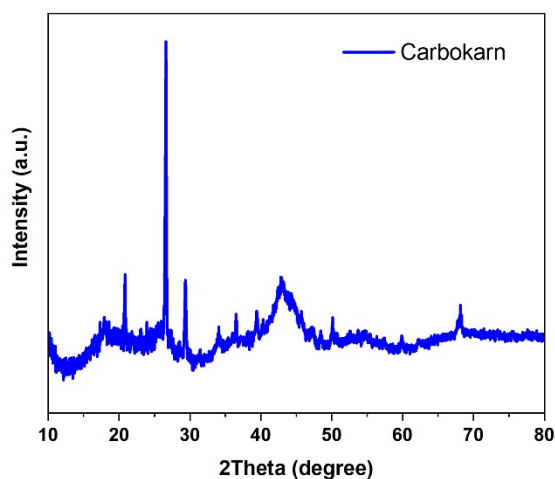


Figure S3. EDX elemental mapping of A), OPL_HTC, B) OPL_KOH11, C) OPL_KOH12 and D) OPL_KOH13

Figure S4. X-ray diffraction (XRD) of the Cabokarn.

X-ray diffraction is used to study the crystalline structure of the as-prepared carbons. According to the (002) and (100) planes of graphite, Carbokarn (commercial activated



carbon) have two large diffraction peaks at 24° and 43°.

Figure S4. X-ray diffraction (XRD) of the Cabokarn.

Figure S5. CV curves of the as-prepared porous carbons in 1m LiTFSI electrolytes.

To investigate the electrochemical characteristics of the as-prepared porous carbon, cyclic voltammetry was carried out in 1m LiTFSI electrolytes under the potential range -1.1-0.9 V. The corresponding CV curves are shown in Figure S5A-D. All the as-prepared OPL_KOH electrodes show a quasi-rectangular curve, which indicates the EDLC behaviour. However, the small distortion of the CV curve at a very low scan rate is due to the fast ion diffusion and low resistance. When increasing the scan rates, a small distortion of the curves is observed due to the high fraction of micropores which increases the ion diffusion resistance and thereby limits the ion transport into the porous structure. The slight distortion is due to the hierarchical porous structure of the OPL_KOH materials, enabling shorten ion diffusion pathways. In addition, the charge storage mechanism in OPL_HTC is different from others due to the presence of peaks in its CV curve.

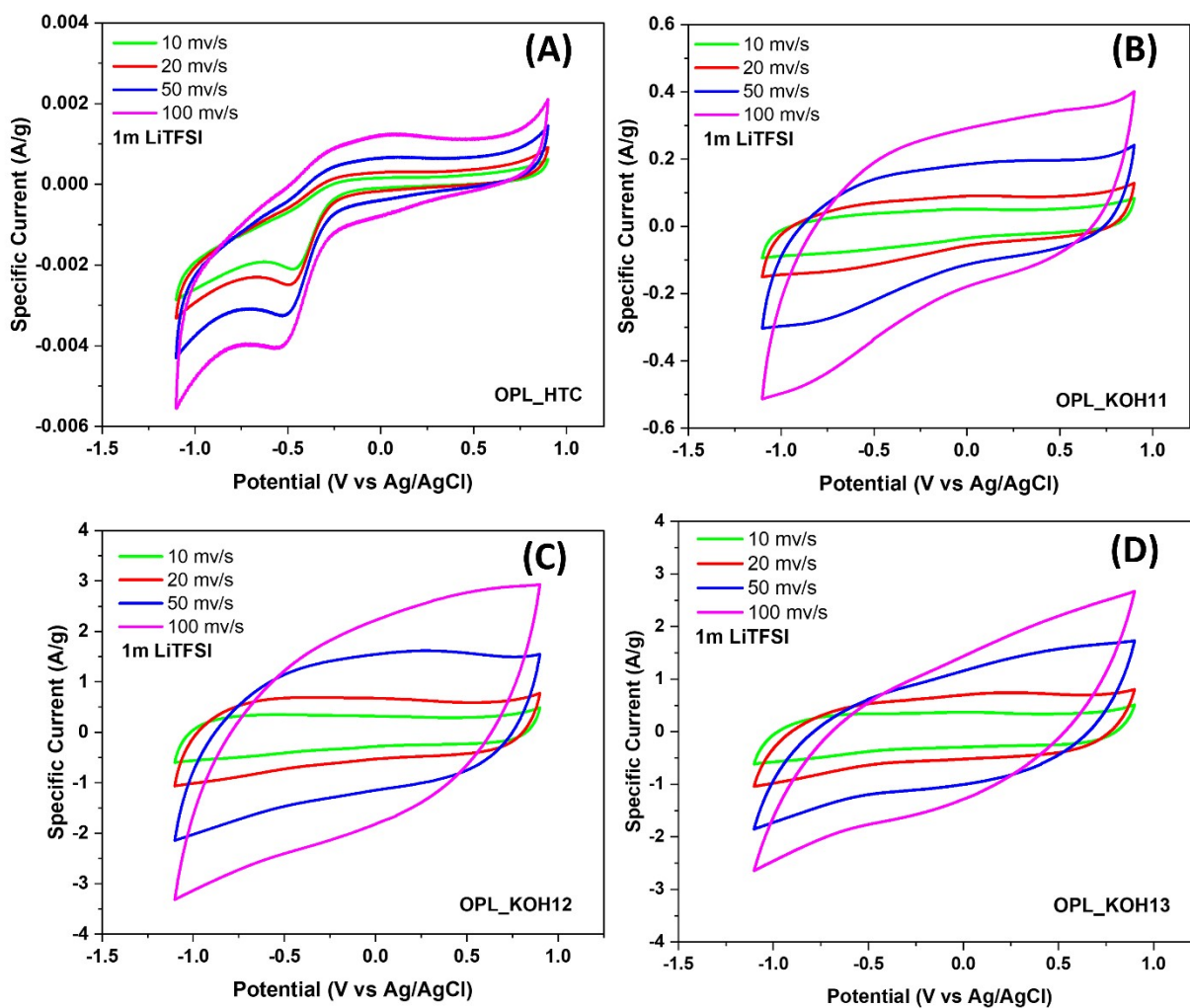


Figure S5. CV curves of A) OPL_HTC, B) OPL_KOH11, C) OPL_KOH12 and D) OPL_KOH13 in 1m LiTFSI electrolytes at a scan rate of 10 to 100 mV/s.

Figure S6. CV curves of the as-prepared materials and the specific capacitance in 1 m LiTFSI electrolyte.

The specific capacitance of the porous carbon electrodes calculated from the area of the CV curves at a low scan rate of 10 mV/s, the specific capacitance of OPL_HTC, OPL_KOH11, OPL_KOH12, OPL_KOH13 is 1, 18, 119 and 113 F/g for, respectively are demonstrated in Figure S6A-B. In general, due to ion diffusion limitation, the specific capacitance of the electrodes gradually decreases when the scan rate increases.

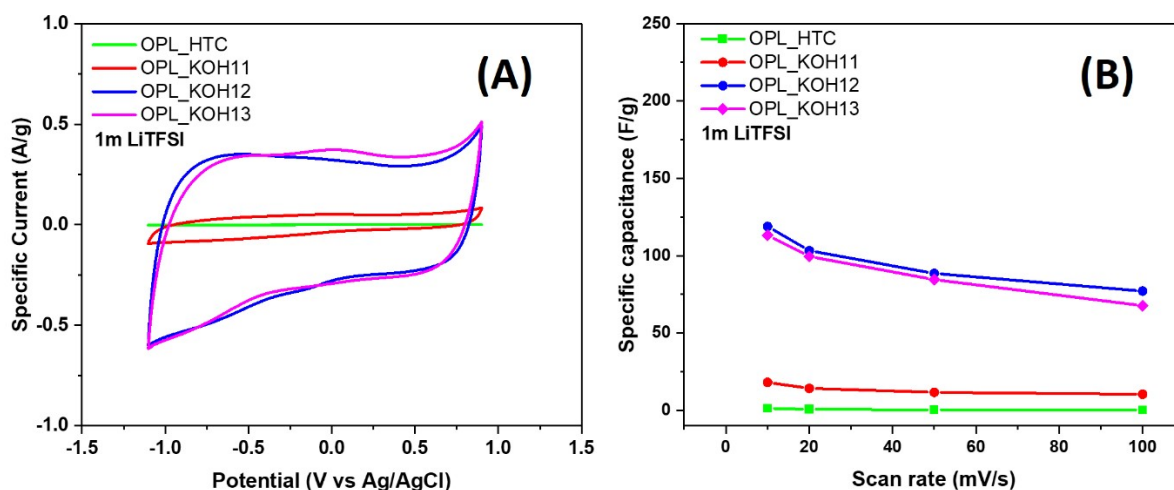


Figure S6. (A) CV curves of the as-prepared materials, (B) the specific capacitance of the as-prepared materials calculated from CV curves versus the scan rate. (All CV results were tested in 1 m LiTFSI)

Figure S7. Nyquist and Bode plots of the as-prepared carbon materials

The Nyquist plot of the materials is presented in Figure S7A. A small semi-circle is observed in the high-frequency region which implies the charge transfer resistance between the electrode and electrolyte interface. In the low-frequency region, the line close to the vertical axis indicates the ideal capacitive behaviour³. The OPL_KOH 12 electrode shows the smallest semi-circle diameter in the high-frequency region, attributing to the lowest charge transfer resistance ($3.84 \Omega \text{ cm}^2$) compared to OPL_HTC ($5.89 \Omega \text{ cm}^2$), OPL_KOH11 ($3.99 \Omega \text{ cm}^2$) and OPL_KOH13 ($4.29 \Omega \text{ cm}^2$). This result confirms the excellent electrical conductivity of the OPL_KOH12 electrode. Also, the oblique line of the OPL_KOH12 curve is closest to the vertical axis in the low-frequency region, demonstrating the fast ion diffusion due to a large number of mesopores in the material. Bode plots exhibit the phase angle of the as-prepared electrodes as a function of frequency (Figure S7B). The phase angle of OPL_HTC, OPL_KOH11, OPL_KOH12 and OPL_KOH13 are 44.53° , 55.94° , 79.48° and 65.14° , respectively. As a result, the phase angles of OPL_KOH12 are close to 90° , suggesting the ideal capacitive behaviour. When the phase angle reaches 45° , the capacitive

and resistive impedances are equal. The characteristic frequency at 45° is known as the knee frequency (f_0) and the relaxation time ($\tau_0 = 1/f_0$) is the minimum time needed to discharge stored energy^{4, 5}. OPL_KOH11, OPL_KOH12 and OPL_KOH13 show τ_0 of 20.83, 4.29 and 15.15 seconds respectively. The low relaxation time of OPL_KOH12 suggests the superior rate capability of the electrode compared to other carbon materials. To further understand the behaviour of the as-prepared carbons, the capacitance is calculated as a function of frequency using Eqn. S1–S2. Figure S7C illustrates the plot between the normalised real-part capacitances and frequencies. Principally, the resistive behaviour is found at high frequencies due to the fast polarisation while the electrode behaves as a capacitor at low frequencies due to the slow polarisation⁶⁻⁸. The transition region from the resistor to the capacitor of OPL_KOH12 is at a higher frequency than other OPL_KOH electrodes, suggesting faster ion diffusion into the material⁸. This could be because the OPL_KOH12 materials have a wide range of pore sizes with high amounts of mesopores, being effective for diffusion. The plot of the normalised imaginary-part capacitance as a function of frequency is shown in Figure S7D. The relaxation time (τ_0) which represents how fast the electrode discharges the stored energy, can also be obtained from the maximum C'' at a certain frequency (f_0)^{6, 8}. The lowest τ_0 can be found for the OPL_KOH12 sample with 4.29 seconds, and the largest τ_0 for the OPL_KOH11 with 100 seconds. Hence, these results confirm the excellent electrochemical performance of the OPL_KOH12 due to its porous structure and high conductivity

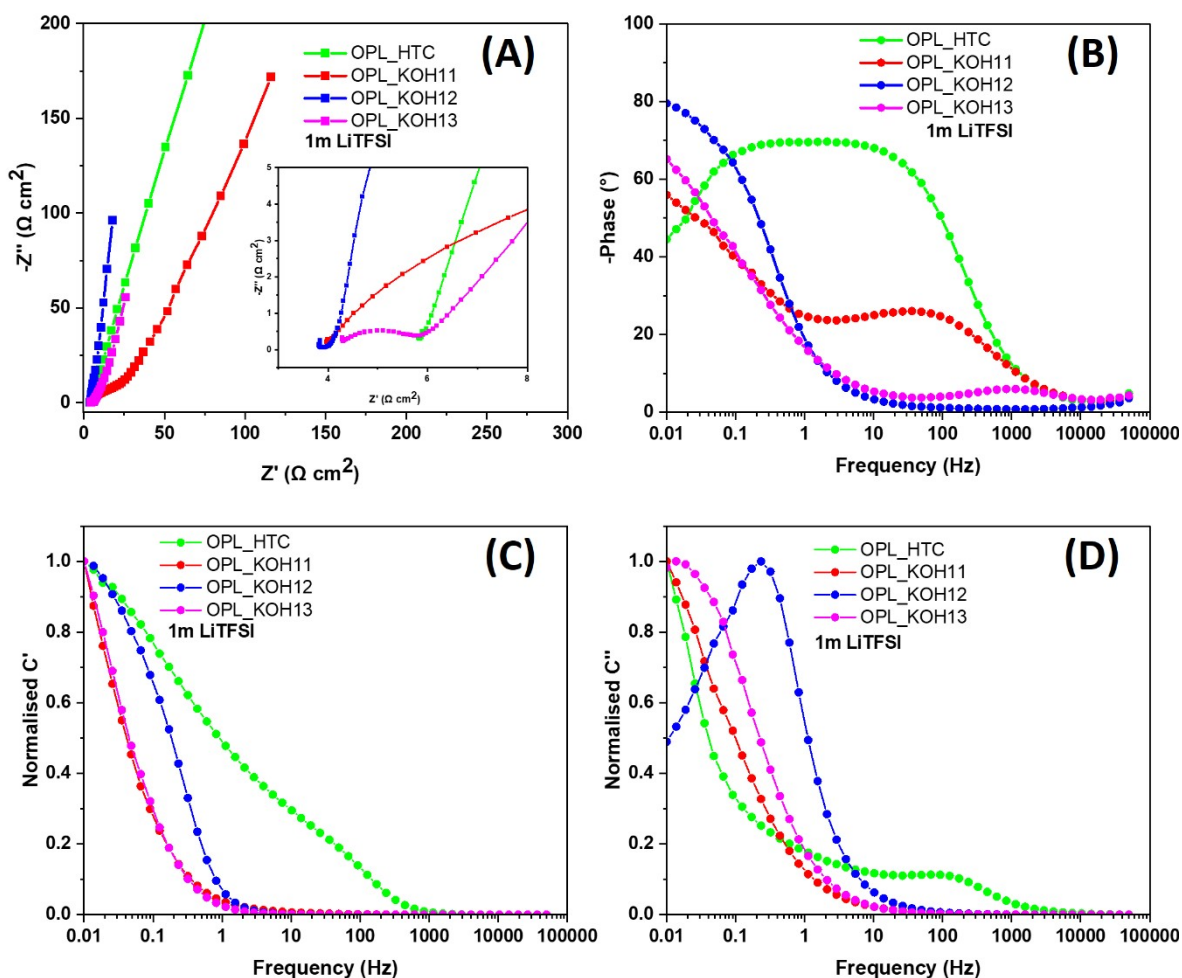


Figure S7. (A) Nyquist plot of the as-prepared materials. (B) Bode plot of the as-prepared materials (C) real and (D) imaginary parts of the normalized capacitances as a function of frequencies (All above results were tested in 1m LiTFSI)

Figure S8. CV curves of the as-prepared porous carbons in 20m LiTFSI electrolytes.

The CV curves of the as-prepared materials tested in 20 m LiTFSI are shown in Figure S8A-D. Excluding OPL_HTC, all materials reveal CV curves with a quasi-rectangular shape. Noted, small humps are sometimes observed due to the gases which are not completely removed from a pre-degassed process. With the use of highly concentrated electrolytes, the operating potential range was broadened to be from -1.3 to 1.3 V.

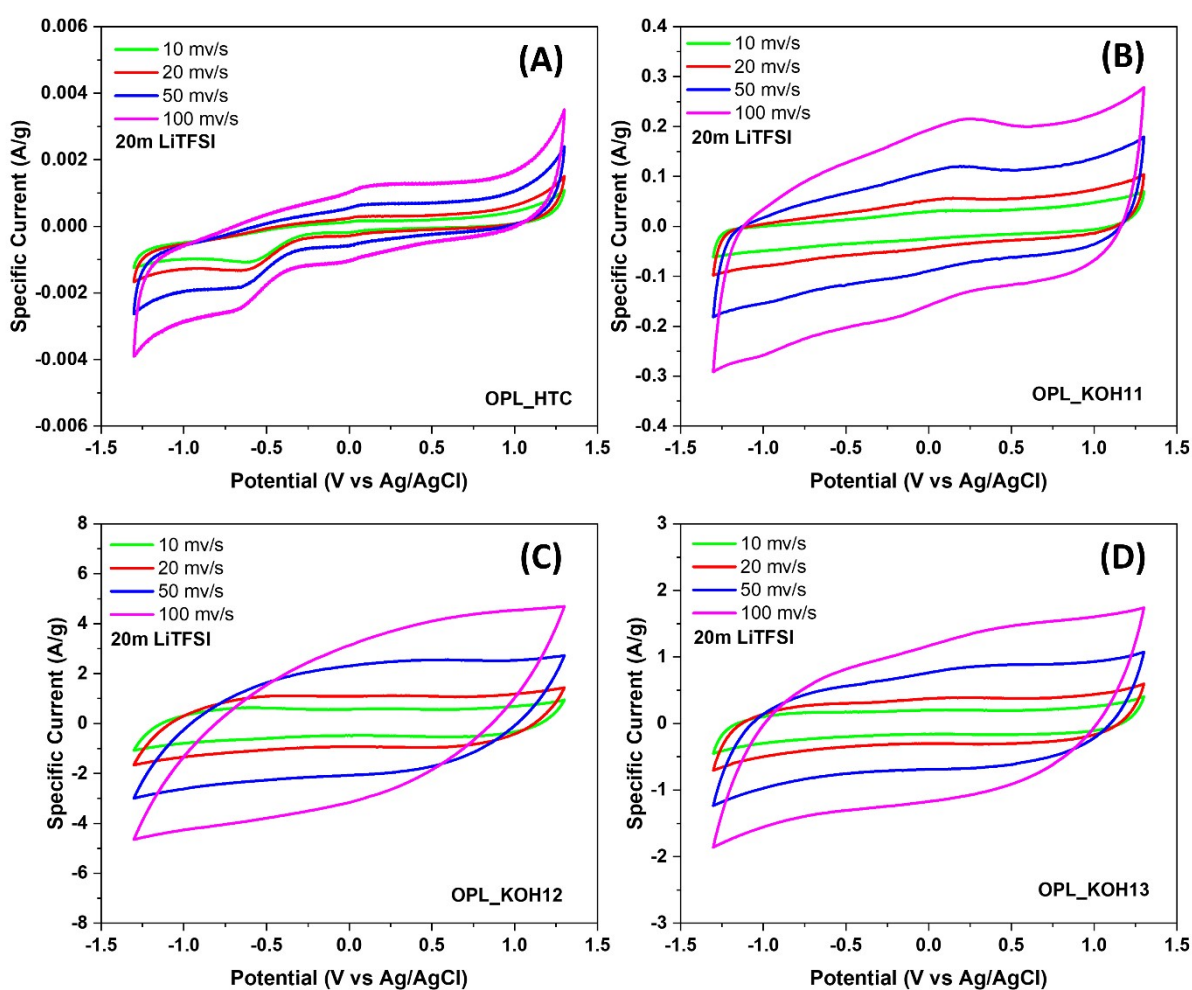
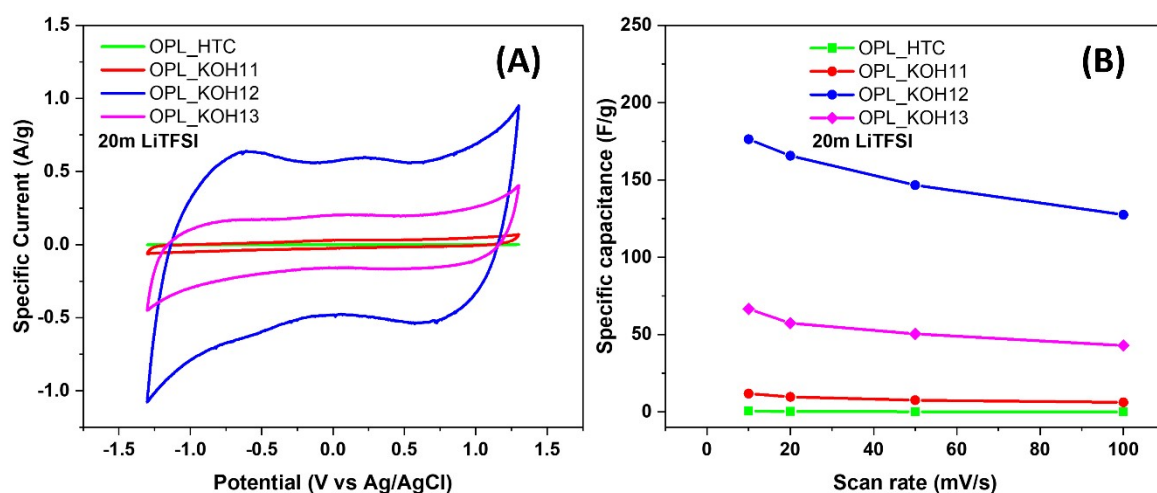


Figure S8. CV curves of A) OPL_HTC, B) OPL_KOH11, C) OPL_KOH12 and D) OPL_KOH13 in 20m LiTFSI electrolytes at a scan rate of 10 to 100 mV/s.

Figure S9. CV curves of the as-prepared materials and the specific capacitance in 20 m LiTFSI electrolyte.

The solvated Li cations become larger in the WIS electrolyte; they are inaccessible into the total subsurface of the material. As shown in Figure S8, the wider operating potential is corresponded to the restriction of the water-splitting reaction due to the scarcity of free water molecules in the 20 m LiTFSI electrolyte; almost all water molecules involve the solvation of Li ions. Also, the reduction of the TFSI anions leads to the upshift of the oxygen evolution potential⁹. The OPL_KOH12 materials shows the highest specific capacitance of

176 F/g at 10 mV/s, while the specific capacitance of OPL_HTC, OPL_KOH11 and



OPL_KOH 13 are 0.5, 12, and 66 F/g, respectively.

Figure S9. (A) CV curves of the as-prepared materials, (B) the specific capacitance of the as-prepared materials calculated from CV curves versus the scan rate. (All CV results were tested in 20 m LiTFSI)

Figure S10. CV curves of the as-prepared porous carbons in 1 m and 20m LiCl and LiTFSI electrolytes.

The CV curves of OPL_KOH12 tested in two different electrolytes are shown in Figure S10A-D. The potential window of the electrode in 1 m LiCl electrolyte is less than that of 1 m LiTFSI electrolyte. Increasing the concentration to 20 m can widen the operating potential to 2 and 2.6 V in LiCl and LiTFSI, respectively.

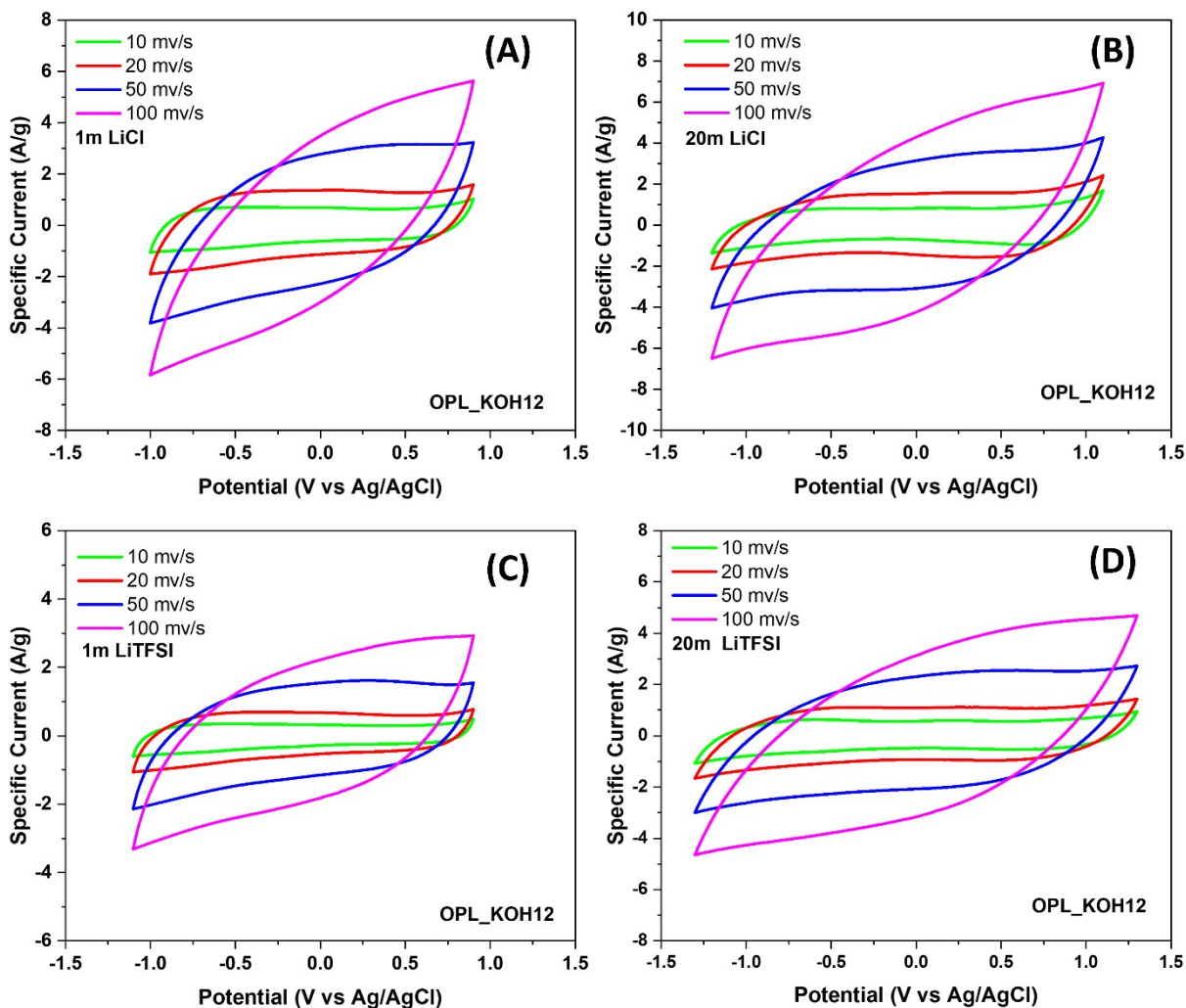


Figure S10. CV curves of OPL_KOH12 tested in A) 1 m LiCl, B) 20 m LiCl, C) 1 m LiTFSI and D) 20 m LiTFSI electrolytes at a scan rate of 10 to 100 mV/s.

Figure S11. Cycling properties of OPL_KOH12 in 1 m and 20m LiCl and LiTFSI electrolytes.

The CV curves of OPL_KOH12 for the five cycles with various electrolyte are illustrated in Figure S11. The OPL_KOH12 showed similar CV curves in each cycle confirming the excellent cycling performance in all electrolytes. The specific capacitance of the OPL_KOH 12 calculated from CV curves are also presented in Figure S12.

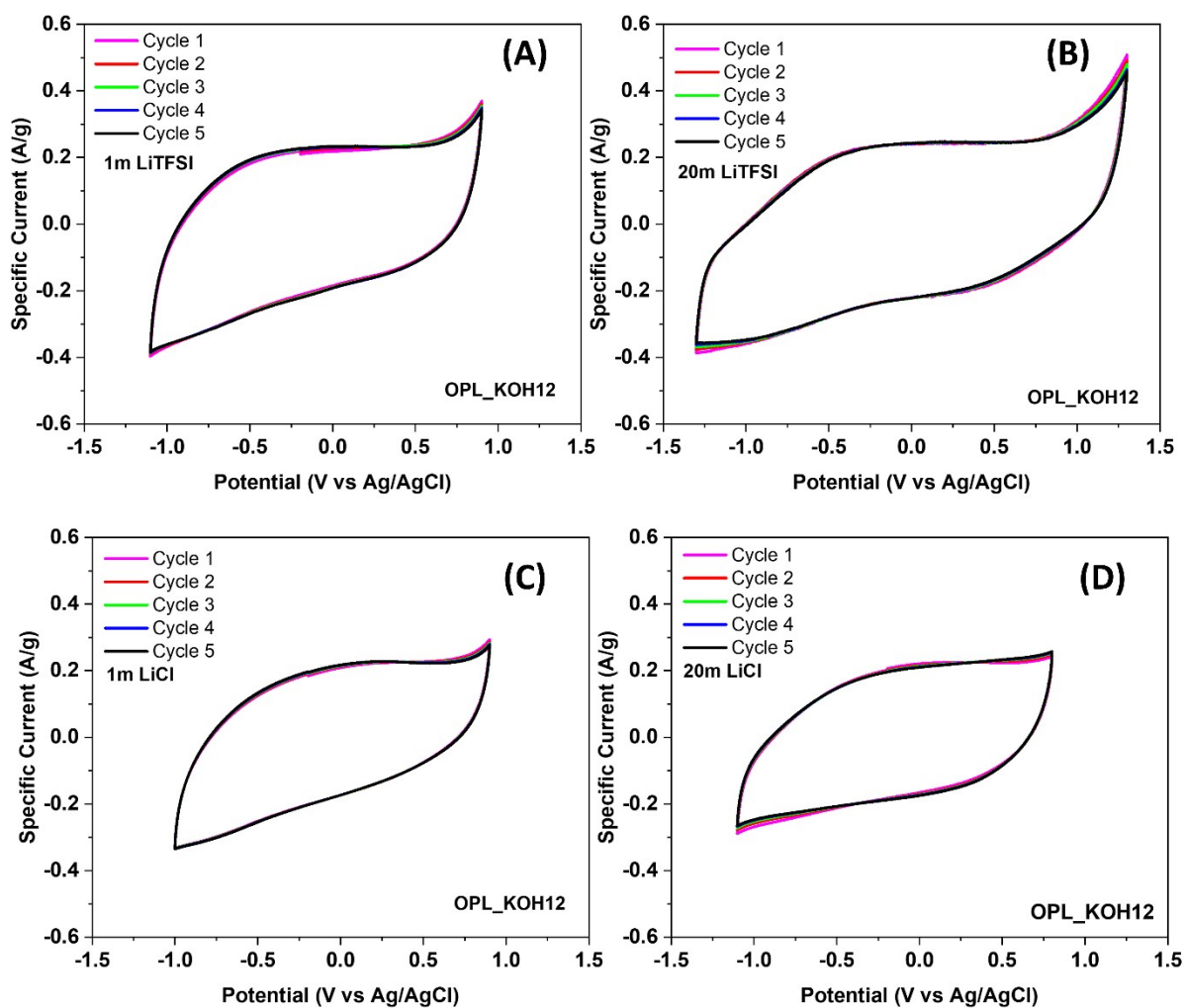


Figure S11. CV curves of OPL_KOH12 tested in A) 1 m LiTFSI, B) 20 m LiTFSI, C) 1 m LiCl and D) 20 m LiCl electrolytes at different cycles. (the three-electrode system)

Figure S12. The calculated specific capacitance versus cycle number in different electrolytes

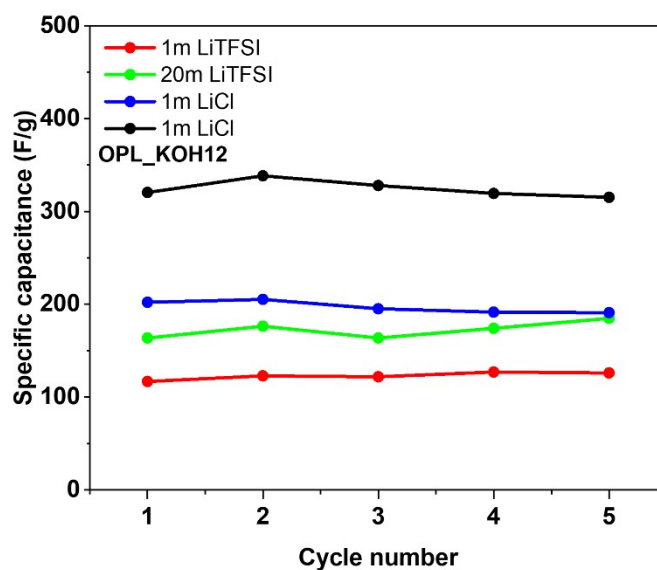


Figure S12. The specific capacitance of the OPL_KOH12 calculated from previous CV curves versus cycle numbers.

Figure S13. Dependence of stored charge versus scan rate in LiCl and LiTFSI electrolytes.

The experiments were carried out at various scan rates to study the charge storage at the inner and outer surfaces. For the $C_{\text{Outer}} (v \rightarrow \infty)$, the plot of the capacitance (C) as a function of the inverse square root of the scan rate ($v^{-1/2}$) is shown in Figure S13A. For the $C_{\text{Total}} (v \rightarrow 0)$, the plot of the inverse capacitance ($1/C$) as a function of the square root of the scan rate ($v^{1/2}$) is exhibited in Figure S13B. Trasatti's method shows a linear correlation between $1/C$ and $v^{1/2}$ (C_{Total}) and C and $v^{-1/2}$ (C_{Outer}). Thus, the C_{Outer} and $1/C_{\text{Total}}$ can be evaluated from the y-intercept of the graph.¹⁰

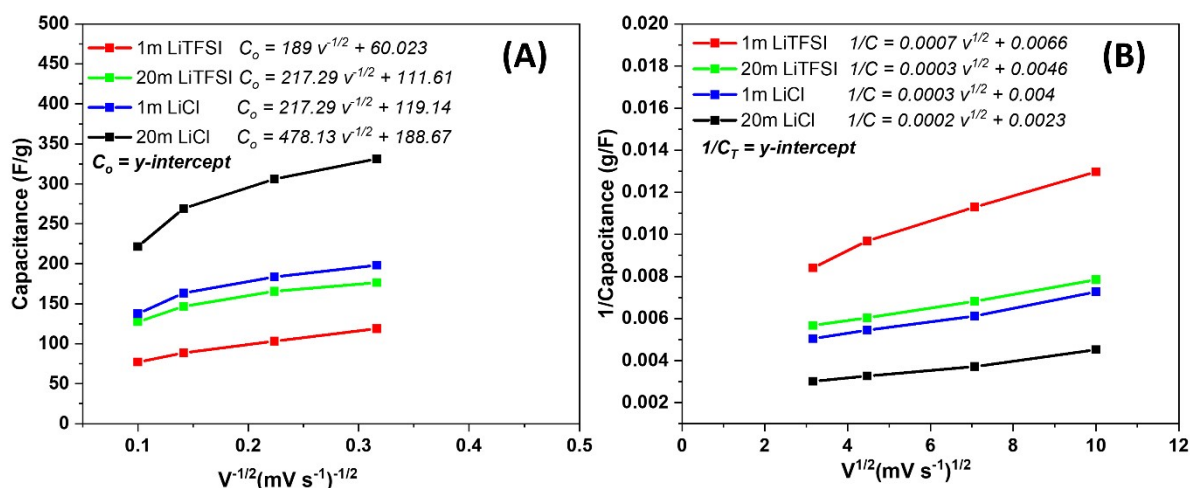


Figure S13. (A-B) dependence of $1/C$ on $v^{1/2}$ and Dependence of capacitance (C) on $v^{-1/2}$ for OPL_KOH12 in 1 m and 20m LiCl and LiTFSI electrolytes at a scan rate of 10 to 100 mV/s.

Figure S14. Cyclic stability of the symmetric coin cells fabricated from the OPL_KOH12 electrode in 20 m LiCl and LiTFSI electrolytes

To study the cycling stability of the OPL_KOH12 electrode in the WIS electrolyte, symmetric coin cells were fabricated using OPL_KOH12 as one electrode and 20 m LiCl and LiTFSI as electrolytes. Galvanostatic charge-discharge cycling was performed at 0.1 A/g (Figure S14). The specific capacitance of OPL_KOH12 after 100 cycles was found to be 77 F/g and 8 F/g in 20 m LiTFSI and LiCl electrolytes, respectively. The symmetric supercapacitor in the WIS LiTFSI electrolyte demonstrated a capacitance retention of 92.9%, while the capacitance retention of the cell in the WIS LiCl was 88.7%.

Unexpectedly, the low specific capacitance and poor retention of the OPL_KOH12 electrode in the 20 m LiCl system during testing the two-electrode system may be attributed to the corrosion of the Al substrate in the acidic environment of the WIS electrolyte. This occurrence was not found when tested in three-electrode system using GCE as a support electrode. This corrosive incident was recently reported by Bunpheng (2023)¹¹. However, these

results clearly highlight the significance of substrate usage in future work when fabricating full cells using LiCl water-in-salt electrolyte. Furthermore, the symmetric device in the 20 m LiTFSI electrolyte delivered a specific energy of 38.7 Wh/kg and a specific power of 380 W/kg, while the specific energy and specific power of the cell in the 20 m LiCl electrolyte were 0.95 Wh/kg and 180 W/kg, respectively.

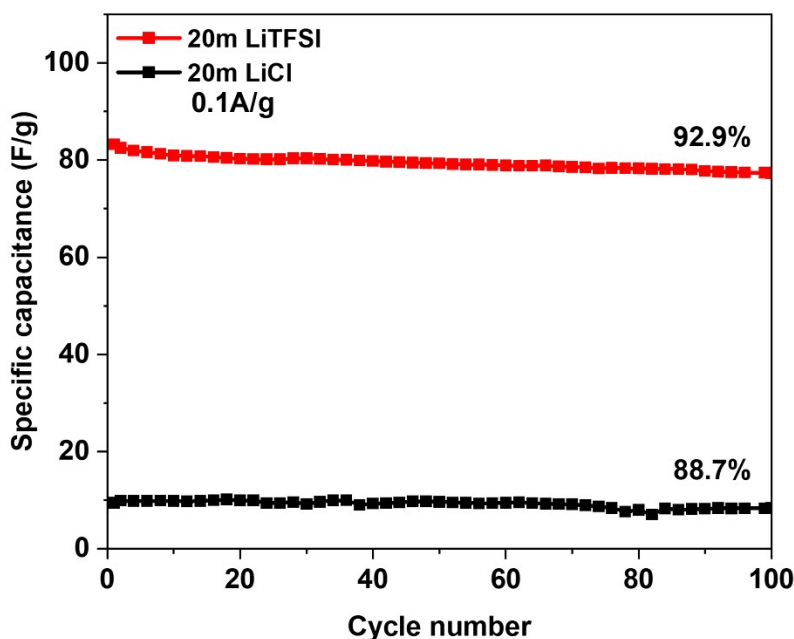


Figure S14. Galvanostatic charge-discharge cycling of the symmetric OPL_KOH12 cells in 20 m LiCl and LiTFSI electrolytes in the voltage range of 0.1-2 (LiTFSI) and 0.1-1 V (LiCl) at a specific current of 0.1 A/g

Figure S15 The XPS spectra of OPL_KOH samples

The composition of the OPL_KOH materials was studied using XPS technique. The survey spectra clearly show the presence of C, O and N elements in the materials. The detailed elements of the OPL_KOH materials were summarised in Table S1. The nitrogen containing functional group also make the OPL_KOH12 more electrochemically active and have a excellent capacitance properties.

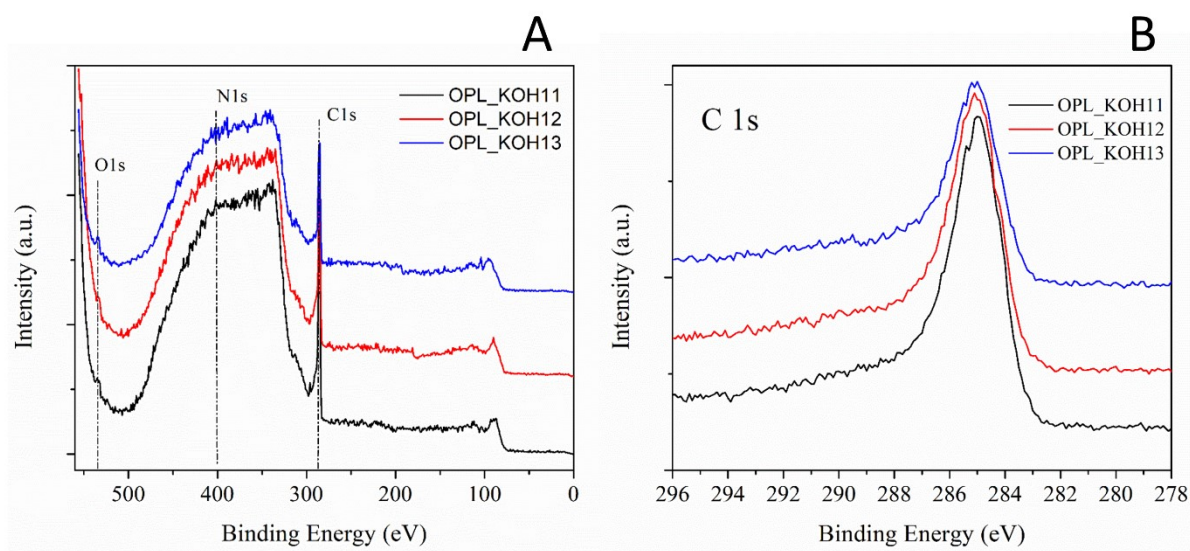


Figure S15. (A) XPS wide spectra of OPL_KOH materials and C1s spectra of the samples

Table S1 XPS analysis data of the OPL_KOH materials

Samples	Atomic Concentration (at%)		
	C1s	O1s	N1s
OPL_KOH11	79.87	4.06	16.08
OPL_KOH12	77.17	1.25	21.58
OPL_KOH13	78.23	4.59	17.17

Table S2 the values from the fitting equivalent circuits (OPL_KOH12 in LiCl and LiTFSI electrolytes)

Sample	R_s (Ω)	R_{ct} (Ω)	CPE1(mF)	CPE2(mF)	Y_0 ($mM\Omega*s^{1/2}$)
1 m LiTFSI	166	171	3.07	12.1	12.1
20 m LiTFSI	197	205	3.11	11.7	13.1
1 m LiCl	104	110	1.94	8.29	13.3

20 m LiCl	108	115	2.18	11.7	9.18
------------------	-----	-----	------	------	------

Supporting Equations

To further analyse the EIS data, the real and imaginary parts of the complex capacitance were calculated by the following Eqn.S1 and S2, respectively

$$C'_{(\omega)} = \frac{-Z''(\omega)}{\omega |Z(\omega)|^2} \quad (S1)$$

$$C''_{(\omega)} = \frac{-Z'(\omega)}{\omega |Z(\omega)|^2} \quad (S2)$$

where Z' and Z'' are the real and imaginary impedance components derived from EIS⁶.

Also, the capacitance is given by Eqn.S3

$$C^{EIS} = \frac{1}{2\pi f Z''} \quad (S3)$$

where f is the frequency of the applied potential harmonic, and Z' are the real impedance components, respectively¹².

ABBREVIATIONS

HTC, hydrothermal carbonization; OPL, oil palm leaves; OPL_HTC, a carbon material prepared from oil palm leaves using hydrothermal carbonization; OPL_KOH11, a carbon material after KOH activation where a weight ratio of the OPL_HTC: KOH (g) was 1:1; OPL_KOH12, a carbon material after KOH activation where a weight ratio of the OPL_HTC: KOH (g) was 1:2; OPL_KOH13, a carbon material after KOH activation where a weight ratio of the OPL_HTC: KOH (g) was 1:3.

SUPPORTING REFERENCES

1. A. Garcia-Maraver, D. Salvachúa, M. J. Martínez, L. F. Diaz and M. Zamorano, *Waste Management*, 2013, **33**, 2245-2249.
2. C. C. de Souza, L. Z. M. de Souza, M. Yilmaz, M. A. de Oliveira, A. C. da Silva Bezerra, E. F. da Silva, M. R. Dumont and A. R. T. Machado, *Cleaner Materials*, 2022, **3**.
3. J. Guo, H. Guo, L. Zhang, B. Yang and J. Cui, *ChemElectroChem*, 2018, **5**, 770-777.
4. X. Liu, C. Ma, J. Li, B. Zielinska, R. J. Kalenczuk, X. Chen, P. K. Chu, T. Tang and E. Mijowska, *Journal of Power Sources*, 2019, **412**, 1-9.
5. T. Purkait, G. Singh, D. Kumar, M. Singh and R. S. Dey, *Scientific Reports*, 2018, **8**, 640.
6. M. A. Bissett, S. D. Worrall, I. A. Kinloch and R. A. W. Dryfe, *Electrochimica Acta*, 2016, **201**, 30-37.
7. P. Chomkhuntod, P. Iamprasertkun, P. Chiochan, P. Suktha and M. Sawangphruk, *Scientific Reports*, 2021, **11**, 13082.
8. L. Borchardt, D. Leistenschneider, J. Haase and M. Dvoyashkin, *Advanced Energy Materials*, 2018, **8**, 1800892.
9. E. Pameté Yambou and F. Beguin, *Electrochimica Acta*, 2021, **389**.
10. S. Ardizzone, G. Fregonara and S. Trasatti, *Electrochimica Acta*, 1990, **35**, 263-267.
11. A. Bunpheng, P. Sakulaue, W. Hirunpinyopas, K. Nueangnoraj, S. Luanwuthi and P. Iamprasertkun, *Journal of Electroanalytical Chemistry*, 2023, **944**, 117645.
12. D. K. Kampouris, X. Ji, E. P. Randviir and C. E. Banks, *RSC Advances*, 2015, **5**, 12782-12791.